Int. J. mech. Sci. Pergamon Press. 1970. Vol. 12, pp. 349–370. Printed in Great Britain

ELASTOPLASTIC ANALYSIS OF PLANE-STRAIN AND AXISYMMETRIC FLAT PUNCH INDENTATION BY THE FINITE-ELEMENT METHOD

C. H. LEE and SHIRO KOBAYASHI
Division of Mechanical Design, Department of Mechanical Engineering,
University of California, Berkeley, California, U.S.A.

(*Received* 18 *December* 1969)

Summary—An elastoplastic analysis of plane-strain and axisymmetric flat punch indentation into a specimen of finite dimensions was made by the finite-element method, using an improved finite-element representation. Studies were made on the development of the plastic zone, the load–displacement relationships, and the stress and strain distributions during continued loading, with variations in the punch friction and specimen dimensions. Unloading was considered also and the residual stresses were examined.

INTRODUCTION

PROBLEMS concerned with indentation have received considerable attention since the investigations of Prandtl[1] in 1920. Prandtl suggested a slip-line field solution for a plane-strain flat punch indentation into a semi-infinite medium, assuming a downward rigid body motion of the material just beneath the punch. Hill[2] pointed out that the velocity distribution in Prandtl's solution was indeterminate, and he proposed a correct solution. For a detailed theoretical analysis of plane-strain flat punch indentation, Hill,[2] Hill *et al.*[3] and Green[4] used the slip-line theory, taking into account the variations in friction and specimen dimensions. An exact solution for axisymmetric indentation by a flat circular punch was given by Shield.[5] For this solution he used the slip-line method based on the Tresca yield and potential functions. These investigations dealt exclusively with rigid–plastic materials with no work-hardening. In a rigid–plastic material no plastic deformation occurs early in the loading path until the plastic zone spreads to a certain critical size when the yield point of the body is reached. At this point the constraint due to the non-plastic part of the material becomes ineffective and distortion begins. In constructing the slip-line field the spread of the plastic zone is usually assumed from experimental observations. The effects of elastic behavior and work-hardening on the yield point load of real materials, although they may be small, are not known. Shaw and DeSalvo[6,7] recently introduced an approximate theory for elastoplastic analysis in an attempt to provide explanations for certain experimental findings in indentation problems. However, a detailed theory for the deformation that takes place during continued loading beyond the yield point is still lacking. Since the growth of the plastic zone from the initial state, and hence its final extent, depends on the path by which the current loading has been reached, it becomes necessary to follow the deformation from moment

to moment, treating the materials as elastic–plastic solids. For this purpose the finite-element method[8] was considered.

The finite-element formulation was developed originally for structural analysis and it has been used for solving many complex structural problems. Although early development of the finite-element method was primarily concerned with linear systems, the method has been extended to non-linear problems by the initial (or thermal) strain method[9,10] or the tangent modulus method.[11,12] Marcal and King[13] introduced a partial stiffness concept and made an elastoplastic analysis of axisymmetric problems as well as problems of plane stress and strain. The most extensive formulation of plane elastoplastic problems appears to be that made by Felippa.[14] He investigated the application of refined displacement, finite elements to the analysis of linear and non-linear problems in structural mechanics. Yamada *et al.*[15] obtained an explicit expression of the incremental stress and strain matrix for the Prandtl–Reuss equations. Their formulation of the matrix is identical to that of Felippa's, but the presentation in the final matrix form differs.

Among the problems solved during the study of the finite-element method were those of Akyuz and Merwin[16] who treated plane-strain indentation for cylindrical indenters, and those of Yamada *et al.*[17] who worked with a flat punch. These examples, however, were given only to demonstrate the problem-solving capability of the method with reference to constant-strain triangular elements. Also, an analysis of axisymmetric indentation was not found by the finite-element method.

This paper, using an improved finite-element representation, deals with a detailed study of plane-strain and axisymmetric flat punch indentation into a specimen of finite dimensions. Development of the plastic zone, the load–displacement relationships and stress and strain distributions during continued loading were studied with variations in friction and specimen dimensions. Unloading was considered also and the residual stresses were examined. The computer programs for elastic analysis with a quadrilateral element composed of four constant-strain triangles[18] and with higher-order quadrilateral finite elements[19] were modified to include the elastoplastic analysis for the present study.

METHOD OF ANALYSIS

A variational formulation for the materials of elastic–plastic behavior in the absence of body forces assumes a stationary value of the functional

$$\Phi = \frac{1}{2}\int_V (\dot{\boldsymbol{\sigma}}^T \dot{\boldsymbol{\varepsilon}})\, dV - \int_S (\dot{\mathbf{U}}^T \dot{\mathbf{F}})\, dS, \tag{1}$$

where $\dot{\boldsymbol{\sigma}}$ is the stress-rate vector; $\dot{\boldsymbol{\varepsilon}}$, the strain-rate vector; $\dot{\mathbf{U}}$, the velocity vector; and $\dot{\mathbf{F}}$, the distribution of the given external stress-rate vector. The superscript T denotes the transpose. The distribution of the stress-rate vector $\dot{\boldsymbol{\sigma}}$ is associated with the strain-rate vector $\dot{\boldsymbol{\varepsilon}}$ which is derivable from a continuous velocity vector $\dot{\mathbf{U}}$, differing infinitesimally from the actual distribution and satisfying the boundary conditions. The surface integral of the second term in (1), while the first integral is taken through the volume of mass, exists only over the part of the surface which is subjected to the stress-rate $\dot{\mathbf{F}}$.

A continuum of elastic–plastic body is divided into M elements interconnected at a finite number of nodal points P. If $\Phi^{(m)}$ is the functional (1) with respect to the mth

element, then

$$\Phi = \sum_{m}^{M} \Phi^{(m)}. \tag{2}$$

The discretization of the variational problem is performed on the elemental level by approximating the functional $\Phi^{(m)}$ by a function $\varphi^{(m)}$ of the mth element nodal point values. This approximation is accomplished by replacing the $\dot{\mathbf{U}}$ distribution with an approximating velocity distribution in each element. Continuity and boundary conditions are the only requirements for admissible distributions of the global variational problem. With this distribution, the functional (1) on the elemental level is expressed by a function $\varphi^{(m)}$. Then, the functional Φ in equation (1) is approximated by the function of P-nodal point variables,

$$\Phi \cong \varphi(\dot{\mathbf{u}}_1, \dot{\mathbf{u}}_2, \ldots, \dot{\mathbf{u}}_P) = \sum_{m}^{M} \varphi^{(m)}(\tilde{\mathbf{u}}_k^{(m)}), \tag{3}$$

where $\dot{\mathbf{u}}_k^{(m)}$ are the values of velocity vectors at nodes in the element. Therefore, the initial variational problem is reduced to determining the location in the P-dimensional vector space of the co-ordinates $\dot{\mathbf{u}}_k$ that minimize $\varphi(\dot{\mathbf{u}}_k)$. The geometric position in the vector space and the elemental distributions then provide the approximate solution to the actual distribution $\dot{\mathbf{U}}$.

The velocity variation on the elemental level is approximated by the function

$$\dot{\mathbf{U}}^{(m)} \cong [N]^{(m)}\, \dot{\mathbf{u}}^{(m)}, \tag{4}$$

where $\dot{\mathbf{u}}^{(m)}$ and $[N]^{(m)}$ are the mth element nodal point values and the mth distribution matrix respectively. When an appropriate operator is applied to the approximated velocities, the strain-rate vector is derivable in the form

$$\dot{\boldsymbol{\varepsilon}}^{(m)} = [B]^{(m)}\, \dot{\mathbf{u}}^{(m)}. \tag{5}$$

For isotropic materials the vectors of rates of stress and strain are associated by Hooke's law in the elastic region and by the Prandtl–Reuss equations during continued loading in the plastic region:

$$\dot{\boldsymbol{\sigma}}^{(m)} = [D]^{(m)}\, \dot{\boldsymbol{\varepsilon}}^{(m)}. \tag{6}$$

The matrix $[D]^{(m)}$ is symmetric. It contains only the material properties of an elastic element, but depends, in addition, on the current states of stress and hardening of the elements in the plastic region. The elemental function $\varphi^{(m)}$, upon substitution of equations (4), (5) and (6) into the functional (1), becomes

$$\varphi^{(m)} = \frac{1}{2}\int_{V^{(m)}} ([D]^{(m)}\,[B]^{(m)}\,\dot{\mathbf{u}}^{(m)})^{\mathrm{T}}[B]^{(m)}\,\dot{\mathbf{u}}^{(m)}\,\mathrm{d}V - \int_{S^{(m)}} ([N]^{(m)}\,\dot{\mathbf{u}}^{(m)})^{\mathrm{T}}\,\dot{\mathbf{F}}^{(m)}\,\mathrm{d}S. \tag{7}$$

Evaluation of surface and volume integrals in equation (7) results in the discrete representation of the functional at the elemental level:

$$\varphi^{(m)} = \tfrac{1}{2}\dot{\mathbf{u}}^{(m)\mathrm{T}}\,[K]^{(m)}\,\dot{\mathbf{u}}^{(m)} - \dot{\mathbf{u}}^{(m)\mathrm{T}}\,\dot{\mathbf{R}}^{(m)}, \tag{8}$$

where $[K]^{(m)}$ is the element stiffness matrix and $\dot{\mathbf{R}}^{(m)}$ is the nodal point force-rate vector equivalent to the external stress-rate $\dot{\mathbf{F}}^{(m)}$ distributed over the surface $S^{(m)}$. The global stiffness matrix $[K]$ and the equivalent nodal point force-rate vector $\dot{\mathbf{R}}$ are the sums of those of the subregions as called for in equation (3). The necessary condition for the function φ to assume a stationary value gives the simultaneous equations for the unknown velocity vectors $\dot{\mathbf{u}}_k$ at the nodes of the region.

When we consider mixed boundary conditions where the velocity vectors over the surface S_U are described, the following matrix equation for the unknown nodal point vectors results:

$$\dot{\mathbf{R}}_a = [K]_{aa}\,\dot{\mathbf{u}}_a + [K]_{ab}\,\dot{\mathbf{u}}_b, \tag{9}$$

where $\dot{\mathbf{R}}_a$ is the known nodal force-rate vector and $\dot{\mathbf{u}}_a$ and $\dot{\mathbf{u}}_b$ are the unknown and prescribed nodal point velocity vectors, respectively. The matrices $[K]_{aa}$ and $[K]_{ab}$ are

the submatrices of the global stiffness matrix $[K]$, according to

$$[K]\dot{\mathbf{u}} = \left[\begin{array}{c|c} [K]_{aa} & [K]_{ab} \\ \hline [K]_{ba} & [K]_{bb} \end{array}\right] \left\{\begin{array}{c} \dot{\mathbf{u}}_a \\ \hline \dot{\mathbf{u}}_b \end{array}\right\}. \tag{10}$$

FORMULATION OF THE STIFFNESS MATRIX

(a) *Plane-strain element*

The elements considered for plane-strain deformation are quadrilateral elements each of which consists of four triangular elements, as shown in Fig. 1. The co-ordinates of a fictitious nodal point 5 are chosen to be the averages of those of nodal points 1, 2, 3 and 4.

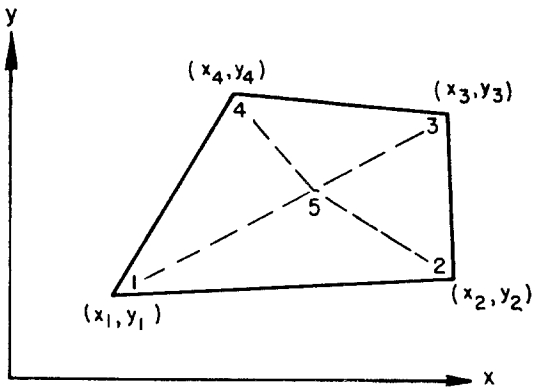

FIG. 1. Plane-strain quadrilateral element.

By assuming a linear velocity distribution within each triangular element and determining the coefficients such that the distribution passes through specified nodal points, the stiffness matrix for each triangular element is first obtained. To formulate the stiffness matrix of the quadrilateral element, the nodal force-rate vectors for four triangular elements are assembled, and the resulting equations are partitioned in the form

$$\left[\begin{array}{cc} [K]_{aa}^{(m)} & [K]_{ab}^{(m)} \\ [K]_{ba}^{(m)} & [K]_{bb}^{(m)} \end{array}\right] \left\{\begin{array}{c} \dot{\mathbf{u}}_a^{(m)} \\ \dot{\mathbf{u}}_b^{(m)} \end{array}\right\} = \left\{\begin{array}{c} \dot{\mathbf{R}}_a^{(m)} \\ \dot{\mathbf{R}}_b^{(m)} \end{array}\right\}, \tag{11}$$

where $\dot{\mathbf{u}}_a^{(m)}$ and $\dot{\mathbf{R}}_a^{(m)}$ are identified by

$$\dot{\mathbf{u}}_a^{(m)} = \left\{\begin{array}{c} \dot{\mathbf{u}}_1^{(m)} \\ \dot{\mathbf{u}}_2^{(m)} \\ \dot{\mathbf{u}}_3^{(m)} \\ \dot{\mathbf{u}}_4^{(m)} \end{array}\right\} \quad \text{and} \quad \dot{\mathbf{R}}_a^{(m)} = \left\{\begin{array}{c} \dot{\mathbf{R}}_1^{(m)} \\ \dot{\mathbf{R}}_2^{(m)} \\ \dot{\mathbf{R}}_3^{(m)} \\ \dot{\mathbf{R}}_4^{(m)} \end{array}\right\}$$

and $\dot{\mathbf{u}}_b^{(m)}$ and $\dot{\mathbf{R}}_b^{(m)}$ are the velocity vector and the nodal force-rate vector respectively at nodal point 5. Eliminating the nodal point variable $\dot{\mathbf{u}}_b^{(m)}$ from equation (11), the stiffness matrix $[K]^{(m)}$ of the quadrilateral element becomes

$$[K]^{(m)} = [K]_{aa}^{(m)} - [K]_{ab}^{(m)}([K]_{bb}^{(m)})^{-1}[K]_{ba}^{(m)}, \tag{12}$$

where $([K]_{bb}^{(m)})^{-1}$ denotes the inverse of the matrix $[K]_{bb}^{(m)}$. After determining the nodal point velocity vectors of the element, the strain-rate vectors in each triangle can be calculated, and the average of the strain-rate values of four triangles evaluated at nodal point 5 is assigned as the value of the strain-rate vector of the quadrilateral element.

(b) *Axisymmetric element*

Elements generally used for the finite-element representation of an axisymmetric body are quadrilateral rings each of which is composed of four triangular rings with linear velocity distributions similar to those discussed for plane-strain elements. Some investigations have been made to improve the accuracy of the finite-element solutions, in particular for axisymmetric deformation problems. The velocity distribution function

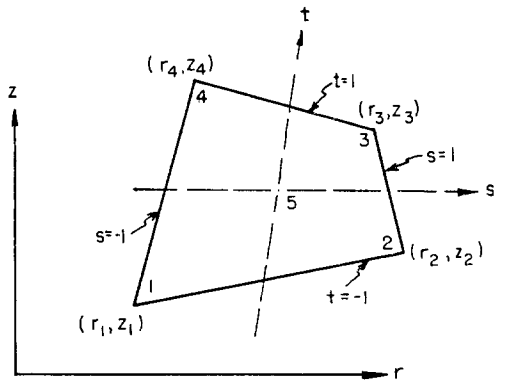

FIG. 2. Axisymmetric quadrilateral element and natural co-ordinate system.

considered here is the one used by Doherty *et al.*[19] The velocity components $\dot{u}_r$ and $\dot{u}_z$ in the radial and axial directions in a quadrilateral element, shown in Fig. 2, are assumed to be

$$\left.\begin{aligned}\dot{u}_r(s,t) &= \sum_{i=1}^{4} q_i \dot{u}_{r_i} + (1-s^2)(1-t^2)\dot{u}_{r_c},\\ \dot{u}_z(s,t) &= \sum_{i=1}^{4} q_i \dot{u}_{z_i} + (1-s^2)(1-t^2)\dot{u}_{z_c},\end{aligned}\right\} \tag{13}$$

where (s,t) represents a natural co-ordinate system, $\dot{u}_{r_i}$ and $\dot{u}_{z_i}$ are the velocity components at the nodal points of the element, and $\dot{u}_{r_c}$ and $\dot{u}_{z_c}$ are those associated with a point within the element (say, the origin of the natural co-ordinate system). The (s,t) co-ordinate system is defined by a transformation with the cylindrical co-ordinate system (r,z) according to

$$r(s,t) = \sum_{i=1}^{4} q_i r_i \quad \text{and} \quad z(s,t) = \sum_{i=1}^{4} q_i z_i, \tag{14}$$

where

$$q_1 = \tfrac{1}{4}(1-s)(1-t), \quad q_2 = \tfrac{1}{4}(1+s)(1-t),$$
$$q_3 = \tfrac{1}{4}(1+s)(1+t), \quad q_4 = \tfrac{1}{4}(1-s)(1+t).$$

From the velocity distribution of equation (13), the strain-rate components are derivable and the strain-rate matrix $[B]^{(m)}$ can be obtained. The element stiffness matrix is then expressed by

$$[K]^{(m)} = 2\pi \iint [B]^{(m)\mathrm{T}} [D]^{(m)} [B]^{(m)} r \, \mathrm{d}r \, \mathrm{d}z. \tag{15}$$

Since the matrix $[B]^{(m)}$ is expressed in terms of (s,t) variables, it is convenient to change the variables r and z in equation (15) to variables s and t. Equation (15) becomes

$$[K]^{(m)} = 2\pi \int_{-1}^{1}\int_{-1}^{1} [B]^{(m)\mathrm{T}} [D]^{(m)} [B]^{(m)} r \, |J(s,t)| \, \mathrm{d}s \, \mathrm{d}t, \tag{16}$$

where $J(s,t)$ is the Jacobian of the transformation of equation (14). The stiffness matrix of the element given by equation (16) is now evaluated by a numerical integration method. For the complete formulation of the stiffness matrix, it remains only to obtain the stress–strain matrix $[D]^{(m)}$.

(c) *Stress–strain matrix*

The formulation of the stress–strain matrix $[D]^{(m)}$ is based on Hooke's law and the Prandtl–Reuss equations. For the elastic state of an isotropic body,

$$\dot{\varepsilon}^e_{ij} = \frac{\dot{\sigma}'_{ij}}{2G} + \delta_{ij}(1-2\nu)\frac{\dot{\sigma}_m}{E}, \tag{17}$$

where $\dot{\sigma}'_{ij}$ is the deviatoric stress-rate tensor; $\dot{\varepsilon}^e_{ij}$, the elastic strain-rate tensor; $\dot{\sigma}_m$, mean stress rate; G, shear modulus; E, Young's modulus; ν, Poisson's ratio; and δ_{ij}, Kronecker's delta. Inverting equation (17), we have

$$\dot{\sigma}_{ij} = 2G\left(\dot{\varepsilon}^e_{ij} + \delta_{ij}\frac{\nu}{1-2\nu}\dot{\varepsilon}^e_{ii}\right). \tag{18}$$

For the elements in the plastic region the plastic stress–strain matrix should replace the elastic stress–strain matrix formed in equation (18). The Prandtl–Reuss equations with the von Mises criterion during continued loading are given by

$$\left.\begin{aligned} \dot{\varepsilon}'_{ji} &= \sigma'_{ij}\dot{\lambda} + \frac{\dot{\sigma}'_{ij}}{2G}, \\ \dot{\varepsilon}_{ii} &= \frac{1-2\nu}{E}\dot{\sigma}_{ii}, \quad \sigma'_{ij}\sigma'_{ij} = \tfrac{2}{3}\bar{\sigma}^2, \end{aligned}\right\} \tag{19}$$

where $\dot{\lambda} = \frac{3}{2}(\dot{\bar{\sigma}}/\bar{\sigma}H')$ and $\dot{\varepsilon}'_{ij}$, $\dot{\sigma}'_{ij}$ are the deviatoric strain-rate tensor and the deviatoric stress-rate tensor respectively. H' corresponds to the slope of the effective stress and plastic strain curve expressed by $\bar{\sigma} = H(\int \mathrm{d}\bar{\varepsilon}^P)$. From equation (19) the plastic stress–strain matrix is obtained according to

$$\dot{\sigma}_{ij} = 2G\left(\dot{\varepsilon}_{ij} + \delta_{ij}\frac{\nu}{1-2\nu}\dot{\varepsilon}_{ii} - \sigma'_{ij}\frac{\sigma'_{kl}\dot{\varepsilon}_{kl}}{S}\right), \tag{20}$$

where $S = \frac{2}{3}\bar{\sigma}^2[1 + (H'/3G)]$.

COMPUTATION PROCEDURES

(a) *Continued loading*

A step-by-step incremental method was employed for the solution of the non-linear equation $[K]\dot{\mathbf{u}} = \dot{\mathbf{R}}$. Existing digital computer programs for plane-strain[18] and axisymmetric[19] elastic problems were modified for the elastoplastic analysis. The sequence of the computer program is as follows:

(1) Apply a unit punch displacement and compute $\Delta\mathbf{u}$, $\boldsymbol{\varepsilon}^e$, $\bar{\sigma}$ and $\boldsymbol{\sigma}$.

(2) Find the element which has a maximum $\bar{\sigma}$ (say, the jth element). Calculate a scale factor η according to $\eta = Y/\bar{\sigma}^{(j)}$. Then multiply $\Delta\mathbf{u}$, $\boldsymbol{\varepsilon}^e$, $\boldsymbol{\sigma}$ and $\bar{\sigma}$ by the scale factor η to obtain the values corresponding to those at the elastic limit. The jth element will be treated as a yielded element for the subsequent computation.

(3) Add $\Delta\mathbf{u}$ to the initial co-ordinates of the nodal points in order to follow the path of deformation.

(4) Apply an incremental punch displacement and compute the corresponding values of $\Delta\mathbf{u}$, $\Delta\boldsymbol{\varepsilon}$ and $\Delta\boldsymbol{\sigma}$. The element stiffness matrices for the yielded elements are calculated based on the previous stress state.

(5) Add $\Delta\boldsymbol{\sigma}$ to the previous $\boldsymbol{\sigma}$ and compute $\bar{\sigma}$ from the resulting $\boldsymbol{\sigma}$.

(6) Find the element having a maximum $\bar{\sigma}$ (say, the kth element) among the elements that have not yielded. Calculate the scale factor by $\eta = 1 - [(\bar{\sigma}^{(k)} - Y)/\bar{\sigma}^{(k)}]$, where $\bar{\sigma}^{(k)}$ is the difference of the effective stresses calculated in step (5) and in the previous stage.

(7) If η is larger than some prescribed value which limits the amount of incremental punch displacement, make η equal to the prescribed value.

(8) Multiply $\Delta\mathbf{u}$, $\Delta\boldsymbol{\sigma}$ and $\Delta\boldsymbol{\varepsilon}$ by η and add to the previous values. Calculate $\bar{\sigma}$ from the resulting $\boldsymbol{\sigma}$. Also calculate $\Delta\bar{\varepsilon}$ from the resulting $\Delta\boldsymbol{\varepsilon}$ and add to the previous value of $\bar{\varepsilon}$.

(9) Check if $\bar{\sigma}$ of any element remaining in the elastic state has reached $0{\cdot}995Y$. The elements having $\bar{\sigma}$ equal to or larger than $0{\cdot}995Y$ will be treated as yielded elements in the next step and thereafter.

(10) Repeat (4) through (9).

(b) *Unloading*

The yield stresses $Y^{(n)}$ of elements after continued loading has stopped are the current values of the effective stresses for the elements that deformed plastically and are equal to the initial yield stresses Y for other elements. If a stress reversal takes place during unloading, the Bauschinger effect must be taken into consideration.

(1) For computation of the first unloading step, consider all elements to be elastic, and compute $\Delta\boldsymbol{\varepsilon}$, $\Delta\boldsymbol{\sigma}$, $\Delta\bar{\sigma}$, $\Delta\mathbf{R}$ and $\Delta\mathbf{u}$, based on the current state of stress and geometry with a unit positive punch displacement (in the direction of unloading).

(2) If $\Delta\bar{\sigma}^{(n)}$ of any element that yielded during loading is positive, repeat (1), treating that element as plastic. This element is to be taken as plastic for the subsequent computation steps as long as $\Delta\bar{\sigma}^{(n)}$ is larger than $(-0{\cdot}001\,Y^{(n)})$ for each unloading stage.

(3) If $\Delta\bar{\sigma}^{(n)}$ of any unyielded element is positive, calculate $\eta^{(n)} = (Y^{(n)} - \bar{\sigma}^{(n)})/\Delta\bar{\sigma}^{(n)}$, where $\bar{\sigma}^{(n)}$ is the effective stress at the previous stage.

(4) Along the punch-workpiece interface, compute the scale factor $\beta^{(i)}$ according to $\beta^{(i)} = -R_z^{(i)}/\Delta R_z^{(i)}$.

(5) Multiply $\Delta\boldsymbol{\varepsilon}$, $\Delta\boldsymbol{\sigma}$, $\Delta\mathbf{R}$ and $\Delta\mathbf{u}$ by the smallest factor among $\eta^{(n)}$, $\beta^{(i)}$ and a prescribed limiting value; then add them to the previous corresponding quantities and calculate the corresponding change in the effective stress $\Delta\bar{\sigma}^{(n)}$.

(6) If $\Delta\bar{\sigma}^{(n)}$ in (5) of any yielded element is less than $-0{\cdot}001\,Y^{(n)}$, ignore computations (3) through (5) and go to (9), treating this element as elastic.

(7) If $\bar{\sigma}$ of any unyielded element reaches $Y^{(n)}$, the element will be treated as plastic in subsequent computations.

(8) If a nodal force in contact with the punch becomes zero, its boundary condition is changed to one having no external force.

(9) For the next unit positive punch displacement, compute all necessary quantities based on the current state of stresses and geometry. Then go to (3).

(10) Repeat (3) through (9) until all nodal forces at the punch–workpiece interface become zero.

RESULTS AND DISCUSSION

A rigid flat punch was indented into a solid specimen of finite dimensions which was placed on a smooth rigid foundation. No separation of the specimen from the foundation was permitted. Thus the solution of the problem also applies to the compression of a specimen between two flat parallel punches. For plane-strain indentation the punch width was $2w$; the specimen width, $2W$; and the specimen height, h with unit thickness. For axisymmetric indentation, $2w$ and $2W$ were the diameters of a circular punch and a solid circular specimen respectively. $W/w = 2{\cdot}7$ for all cases and the depths of the specimens were $h/w = 0{\cdot}6$, $1{\cdot}0$, $1{\cdot}7$ and $2{\cdot}5$. The effect of friction at the punch–workpiece interface was examined also by using a smooth punch and a rough punch (complete sticking). The material properties used for the computation were $E = 10 \times 10^6$ psi, $\nu = 0{\cdot}33$ and $H' = 20{,}000$ psi, with Y (initial yield stress) = 13,000 psi. These values approximated the static stress–strain curve for commercially pure aluminium 1100–0.

Fig. 3 shows the average punch pressures as functions of punch displacement for a smooth punch under plane-strain conditions. The pressure increased linearly first and then the curves showed a rapid bend with a small rate of increase in pressure. The rates of the initial increase in pressure were higher, but the pressures where the curves bend were lower for specimens having less depth. The bends of the load–displacement curves are the yield points of the body and are marked on the curves in Fig. 3. These yield points are compared with those obtained by the slip-line theory for rigid perfectly plastic solids, shown in Fig. 4. The slip-line theory predicts that the pressure for $h/w \leqslant 1{\cdot}0$ is equal to $2k[= (\sqrt{3}/2)\,Y]$ but increases with increasing depth for $h/w > 1{\cdot}0$. It appears that the same conclusion applies to a work-hardening material, as seen in Fig. 4. An interesting study is the effect of friction at the punch–workpiece interface on the load–displacement relationship. Calculations were made for $h/w = 0{\cdot}6$ and $2{\cdot}5$, assuming complete sticking of the workpiece to the punch at the interface, and the results were compared with those found for a smooth punch. For $h/w = 2{\cdot}5$, the load–displacement curve for complete

sticking was identical to that of a smooth punch. On the other hand, a considerable increase in pressure for the sticking friction condition resulted for dimensions of $h/w = 0{\cdot}6$, as shown in Fig. 5. A rough punch requires not only a higher yield-point load but also a

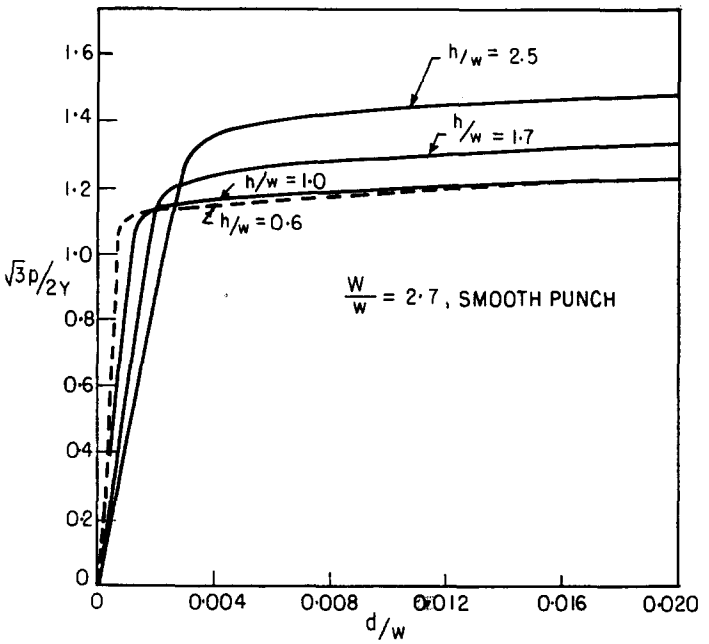

FIG. 3. Plane-strain punch pressure and displacement curves for various depths of specimens with a smooth punch.

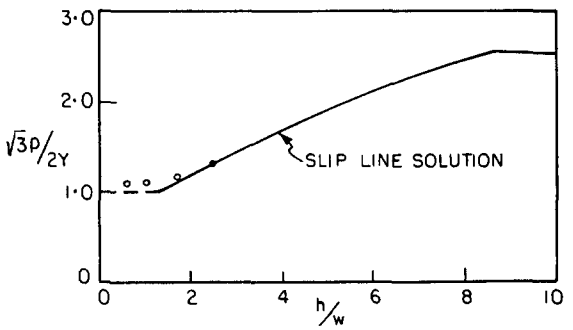

FIG. 4. Yield point pressure as a function of specimen dimensions.

larger rate of increase in pressure after passing the yield point of the body. This result indeed coincides with Bishop's[20] prediction of the effect of friction on the yield-point load. The pressure and displacement curves for axisymmetric indentation with a smooth punch are given in Fig. 6 for various specimen depths. Observations made on the pressure–displacement relationships for plane-strain indentation generally apply also to those under axisymmetric conditions, except that the bends of the curves for the axisymmetric case are not as well defined as those for plane-strain indentation. The effect of friction was examined too by obtaining the solutions for complete sticking conditions for $h/w = 0{\cdot}6$ and 2·5. Again, the pressure–displacement curve was identical to that for a smooth punch

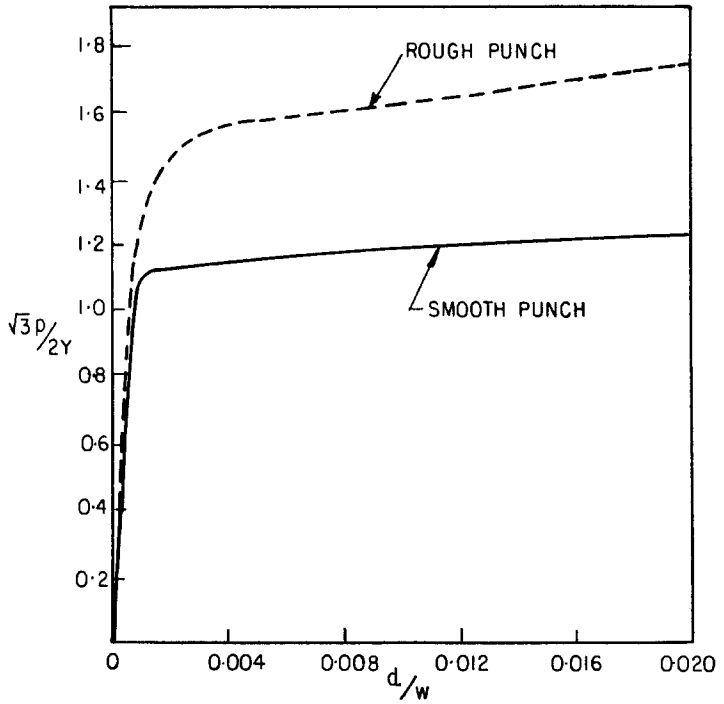

FIG. 5. Effect of punch friction on plane-strain pressure–displacement relationship for $h/w = 0{\cdot}6$.

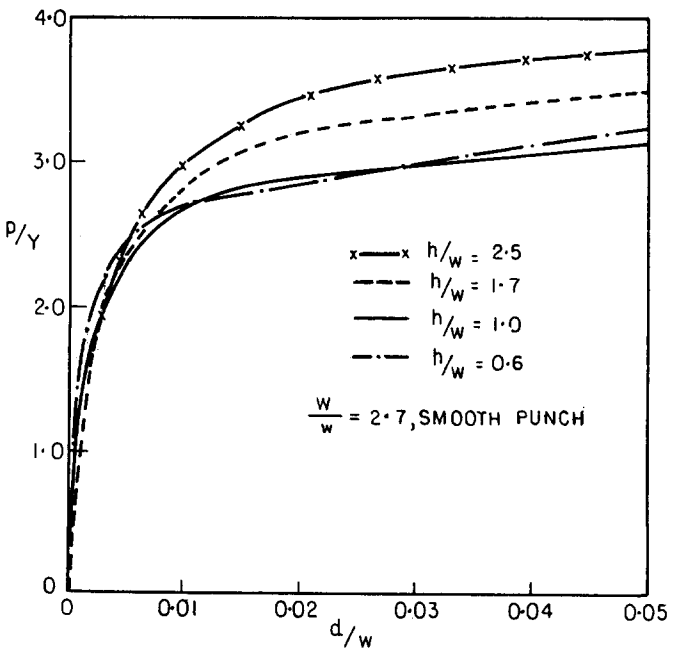

FIG. 6. Axisymmetric punch pressure and displacement curves for various depths of specimens with a smooth punch.

with $h/w = 2{\cdot}5$, but the pressure was higher for a rough punch than for a smooth punch for $h/w = 0{\cdot}6$, as shown in Fig. 7.

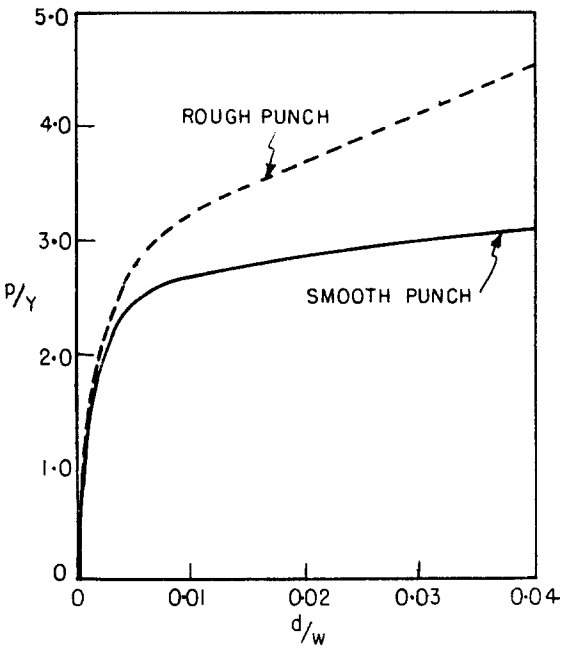

Fig. 7. Effect of punch friction on axisymmetric pressure–displacement relationship for $h/w = 0{\cdot}6$.

A unique feature of the finite-element method is that it permits one to follow the path of deformation from the initial stress-free state. The development of the plastic zone and the manner in which the plastic zone spreads are the important aspects of the solutions. For specimens of small depth, where the punch friction has a considerable effect on the load-displacement curves, the plastic zones in plane-strain indentation for several values of punch displacement d are compared for smooth and rough punches in Fig. 8. The effect of punch friction on the load–displacement relationships is not observed until the plastic zone has developed to a sufficient size. At the yield point [Fig. 8(c)], the elastic zone under the punch formed a double-wedge shape when a smooth punch was used, while a rough punch caused this area to take the shape of a single truncated wedge. When the entire region beneath the punch became plastic, the slope of the load–displacement curve assumed a steady-state value. Fig. 9 shows the plastic zones for $h/w = 1{\cdot}0$, $1{\cdot}7$ and $2{\cdot}7$ at various stages of their development for the indentation with a smooth punch. For all depths of specimens investigated in Fig. 9, the yielding appeared at two locations: one at the corner of the punch and the other at the central bottom of the specimen, as shown in Fig. 9(a). As soon as the plastic zone spread and two yielded zones were connected [Fig. 9(b)], the load–displacement curve began to bend. This connecting plastic zone was wider for larger h/w. At the yield point the truncated wedge-shaped zone under the punch remained elastic, as shown in Fig. 9(c). The plastic zone spread away from the punch during the transition from contained plastic flow to unrestricted flow. The slope of the load–displacement curves then became constant and the plastic zone grew slowly in all directions.

The development of plastic zones in axisymmetric indentation is similar to that for plane strain. Fig. 10 shows a comparison of the development of the plastic zone for smooth and rough punches and it corresponds to Fig. 8 for plane-strain indentation. It is evident that the same observation can be made regarding the effect of punch friction on the formation of the plastic zone. The variations of plastic zone development for

different depths of specimens are shown in Fig. 11. When the plastic zone spread from the corner of the punch to the center of the specimen, the load–displacement curve began to bend. The bend of the curve continued until the plastic zone grew to a sufficient size. Then unrestricted plastic flow became possible. Some variations in the manner of further development of plastic zones for various depths of specimens are seen in Fig. 11. For the dimension $h/w = 1{\cdot}7$ with a smooth punch, an indentation was made up to $d/w = 0{\cdot}15$ for conditions of both plane-strain and axisymmetry, and the effective strain

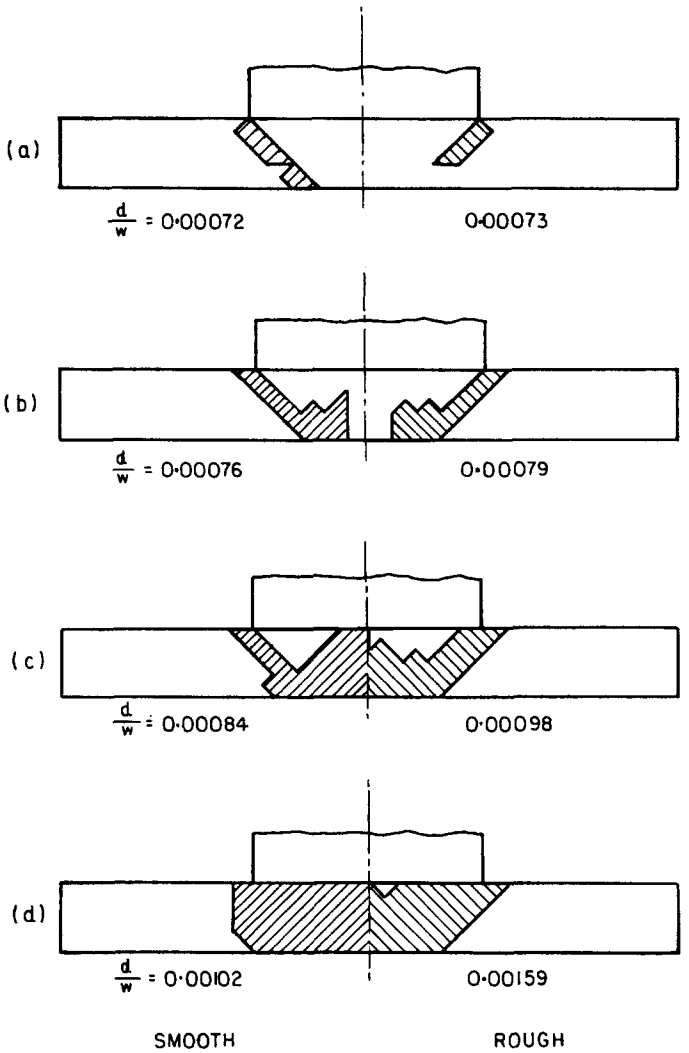

FIG. 8. Effect of punch friction on plastic zone development in plane-strain indentation for $h/w = 0{\cdot}6$.

distributions are shown by constant strain contours in Fig. 12. The effective strain distributions in Fig. 12 reflect the manner in which the plastic zone was developed. Distributions in plane strain and axisymmetry were similar for the same punch displacements except that the whole specimen was in the plastic state for axisymmetry, but an elastic region still existed under the plane-strain condition.

The stress distributions along the punch surface are shown in Fig. 13. The stress values are those at the centers of elements in contact with a rigid smooth punch. Fig. 13(a)

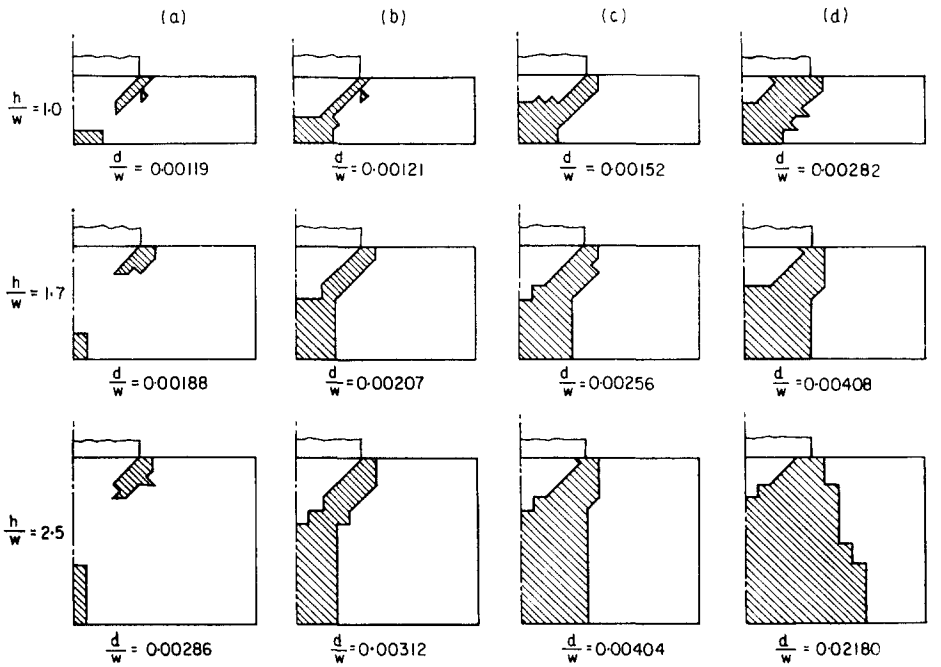

FIG. 9. The growth of plastic zones in plane-strain indentation for various depths of specimens with a smooth punch.

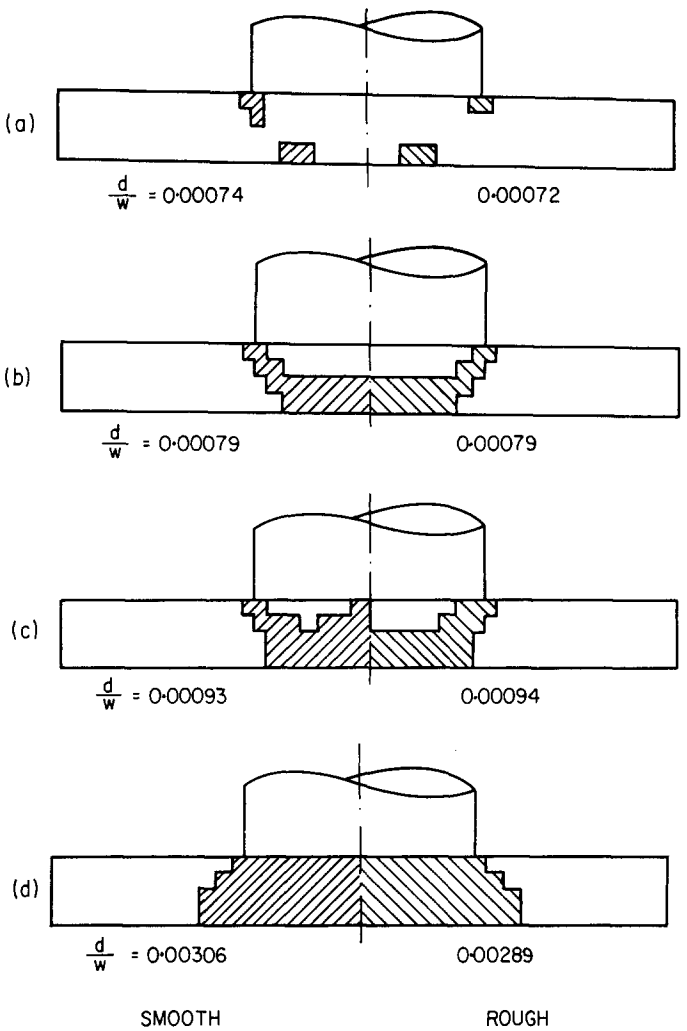

FIG. 10. Effect of punch friction on plastic zone development in axisymmetric indentation for $h/w = 0{\cdot}6$.

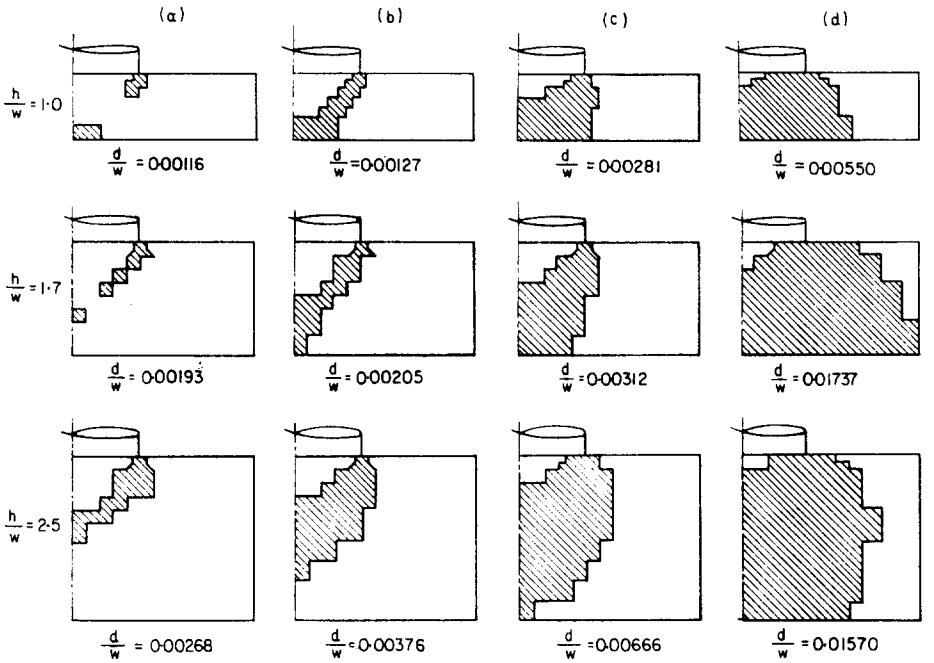

FIG. 11. The growth of plastic zones in axisymmetric indentation for various depths of specimens with a smooth punch.

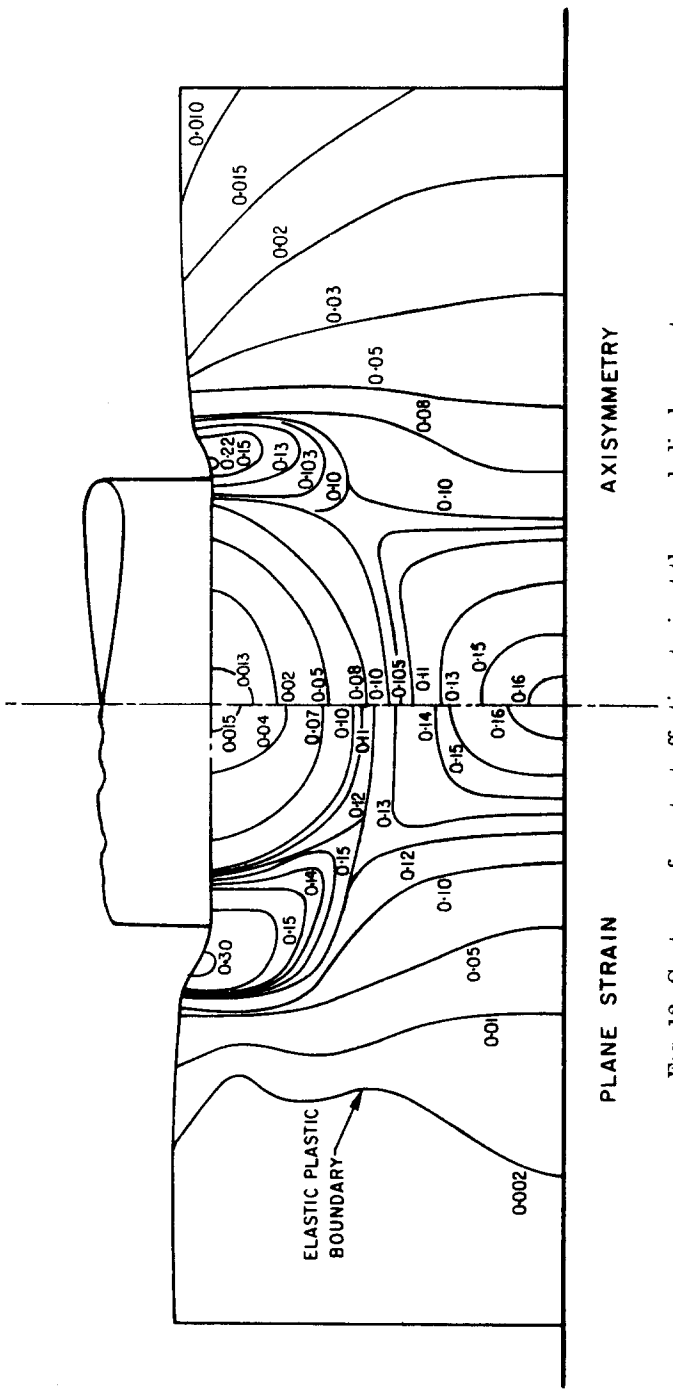

FIG. 12. Contours of constant effective strain at the punch displacement $d/w = 0{\cdot}15$ for $h/w = 1{\cdot}7$ (smooth punch).

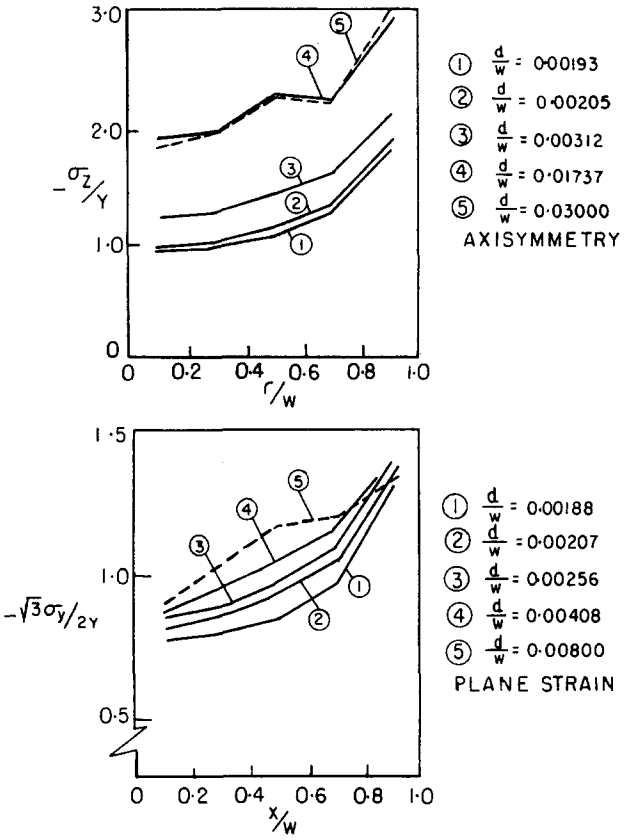

(a)

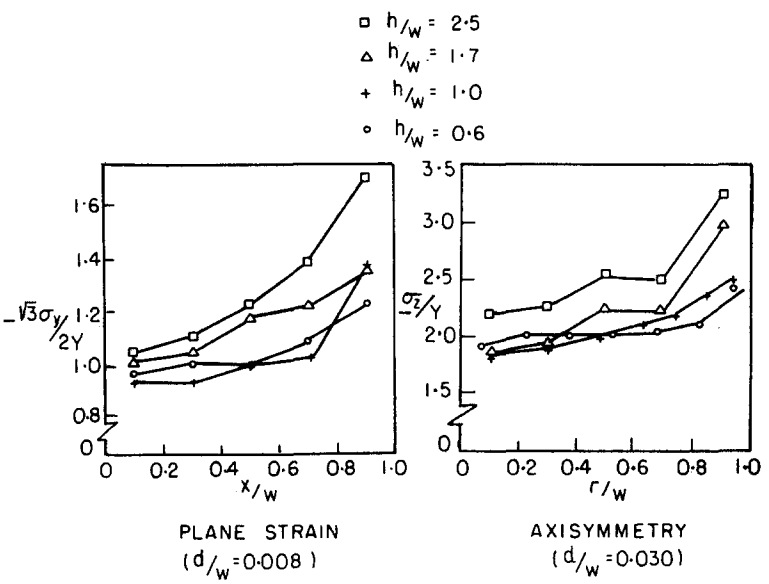

(b)

FIG. 13. Axial stress distributions along the elements in contact with a smooth punch for (a) various punch displacements for $h/w = 1{\cdot}7$ and (b) various specimen dimensions.

shows the distribution for $h/w = 1{\cdot}7$ at various stages of indentation, corresponding to those in Figs. 9 and 11. The stress distribution at a later stage is also added. A trend of the stress distribution is the increase of the magnitude toward the edge of the punch, and it is the same for all cases in plane strain and axisymmetry. The effect of the specimen dimensions on the stress distribution along the punch surface is shown in Fig. 13(b).

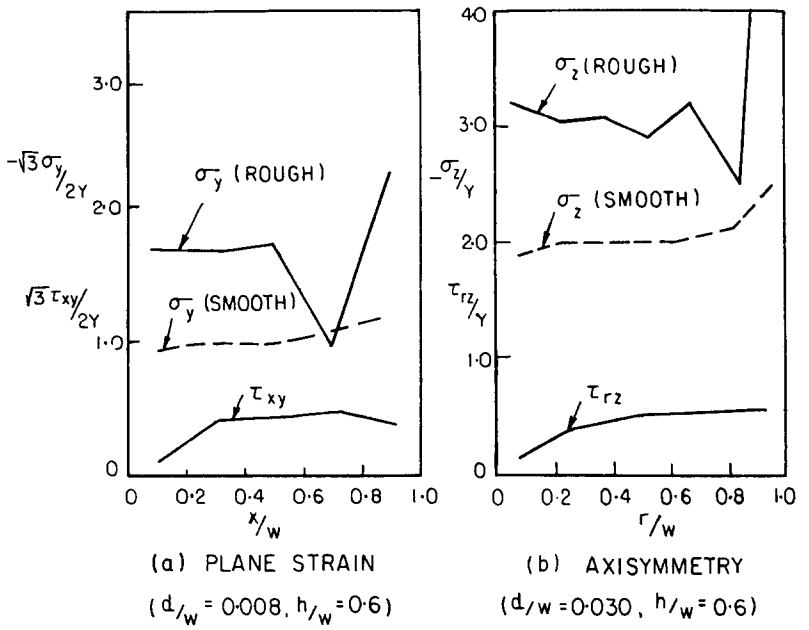

FIG. 14. Comparison of the axial stress distributions along the punch surface for rough and smooth dies with a specimen of $h/w = 0{\cdot}6$.

Fig. 14 gives the stress distributions along the punch surface for rough and smooth dies. Stresses were higher for rough dies than for smooth dies and the stress increase near the punch edge was larger for rough dies. It may be of interest to observe that for rough dies (complete sticking) the shear stresses are almost equal to the initial shear strength over most of the contact surface, but they decrease near the center of the punch. A more detailed examination of the stress distributions was made for axisymmetric indentation with a specimen dimension of $h/w = 1{\cdot}7$ and a punch displacement of $d/w = 0{\cdot}05$, as shown in Figs. 15 and 16. At this punch displacement for axisymmetric indentation, the whole specimen had just become plastic. Fig. 15(a) shows the stress distribution along the elements in contact with the foundation. The hoop stress σ_θ was compressive in the central region but became a tension stress in the outer region of the specimen. The axial stress σ_z was compressive over almost the entire contact surface except that it became tensile near the edge of the specimen. The largest compressive stress occurred at a distance of half the radius of the punch away from the axis of symmetry. The stress distributions along the elements on the axis of symmetry are given in Fig. 15(b). The stresses are all compressive and the largest compressive stress occurred beneath the punch at a distance of half the radius of the punch. The two principal stresses in the (r, z) plane were calculated from the stress components, and the smaller principal stress distribution is shown by the constant stress contours in Fig. 16.

Computation for unloading was performed for axisymmetric indentation for a specimen of $h/w = 1{\cdot}7$ deformed to $d/w = 0{\cdot}15$ with a smooth punch. As soon as removal of the punch began, the state of most of the elements became elastic, except for some elements near the free surface close to the punch edge. They continued to deform plastically. As unloading proceeded some other elements underwent further plastic deformation. This

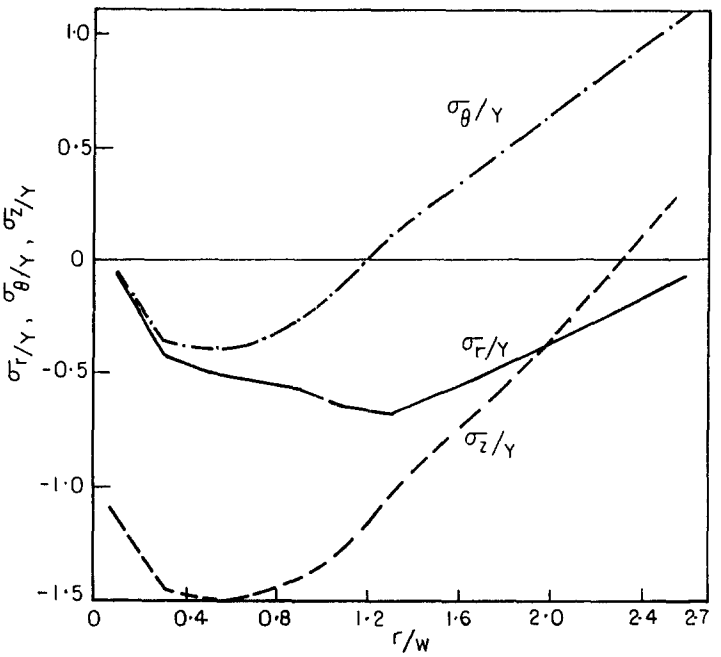

(a)

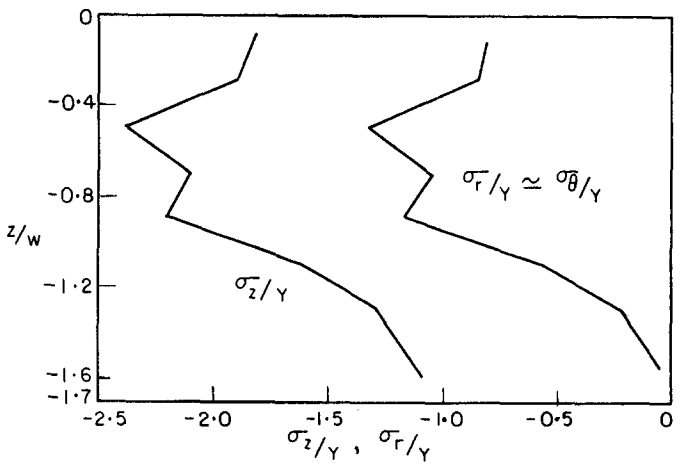

(b)

FIG. 15. Stress distributions for axisymmetric indentation by a smooth punch with $h/w = 1{\cdot}7$ at a punch displacement of $d/w = 0{\cdot}05$. (a) Along the contact surface with the foundation, (b) along the axis of symmetry.

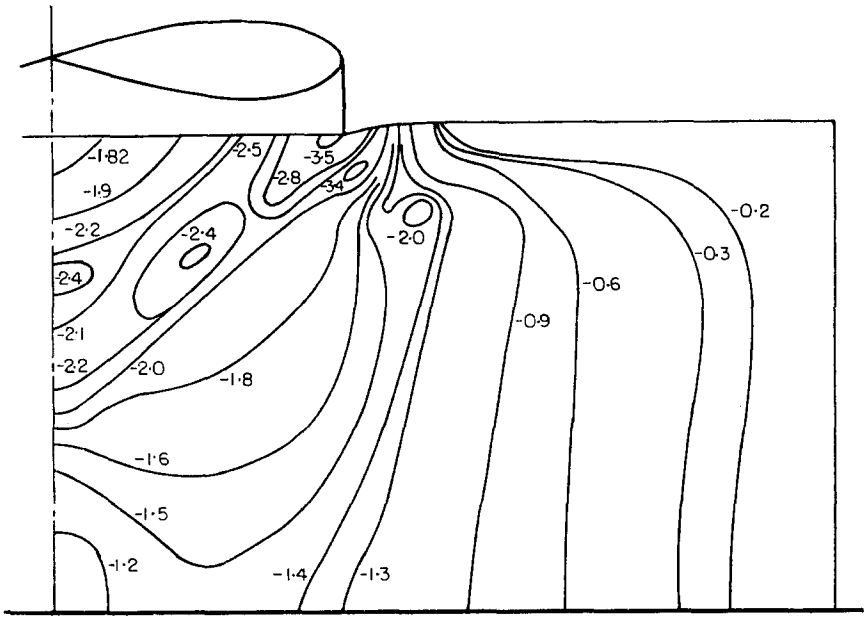

FIG. 16. Constant principal stress (σ_2/Y) contours for axisymmetric indentation by a smooth punch with $h/w = 1{\cdot}7$ at a punch displacement of $d/w = 0{\cdot}05$.

development of the plastic zone during unloading is shown in Fig. 17. At the completion of unloading the total punch displacement (d') in the direction of removal was $d'/w = 0{\cdot}008$. This indicates the amount of springback compared with a total punch displacement of $d/w = 0{\cdot}15$ for loading. The residual stresses after complete unloading together with the stresses before unloading are shown in Fig. 18. The residual stresses along the elements at the bottom surface of the specimen shown in Fig. 18(a) revealed that all the stresses in the central area increase and become tensile as a result of unloading, while the stresses in the outer region decrease slightly. Fig. 18(b) shows the residual stresses along the axis of symmetry. It is interesting to note that the shapes of the distributions are similar to those during loading, but the stresses increase upon unloading and become partly compressive and partly tensile. Axial stress was recovered to a greater extent than radial and hoop stresses. Along the top free surface it was observed that a sharp change in stress distribution existed at the punch edge, as shown in Fig. 18(c). The residual stresses were

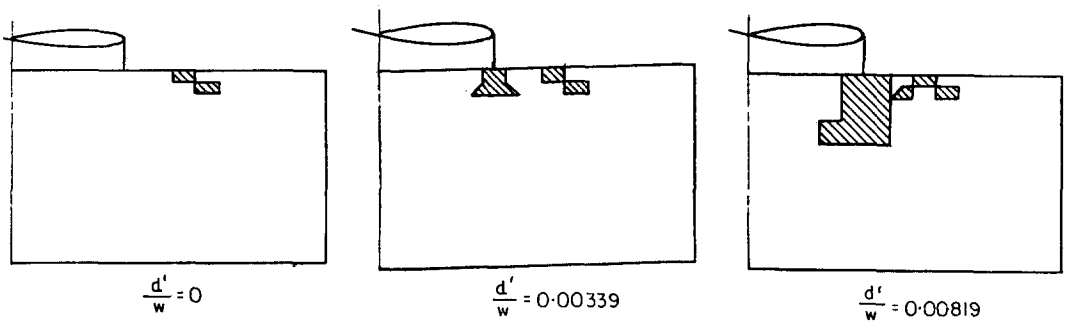

FIG. 17. Plastic zone development during unloading for axisymmetric indentation by a smooth punch with $h/w = 1{\cdot}7$. (Unloading begins at $d/w = 0{\cdot}15$.)

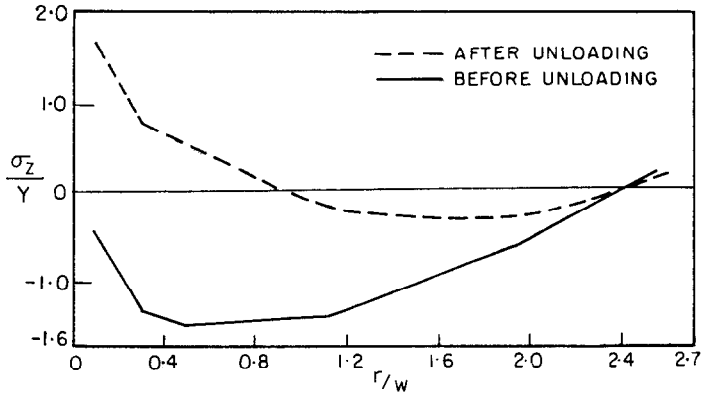
AFTER UNLOADING
BEFORE UNLOADING
σz/Y
2·0
1·0
0
-1·0
-1·6
0
0·4
0·8
1·2
1·6
2·0
2·4
2·7
r/w

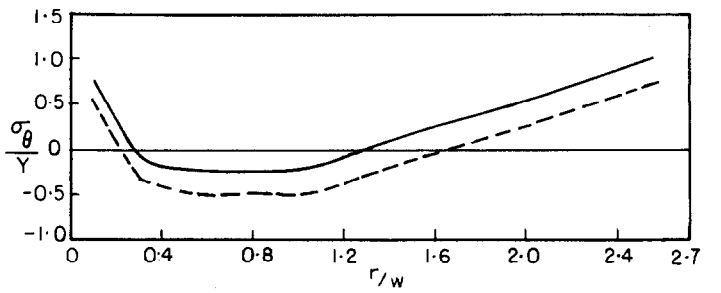
σθ/Y
1·5
1·0
0·5
0
-0·5
-1·0
0
0·4
0·8
1·2
1·6
2·0
2·4
2·7
r/w

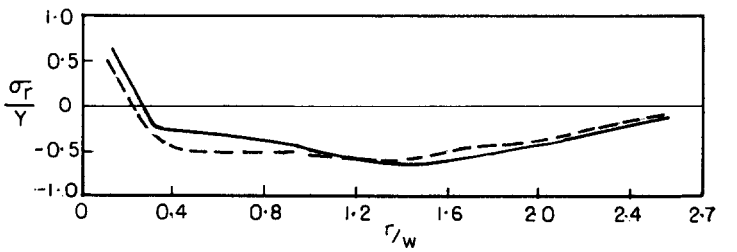
σr/Y
1·0
0·5
0
-0·5
-1·0
0
0·4
0·8
1·2
1·6
2·0
2·4
2·7
r/w

(a)

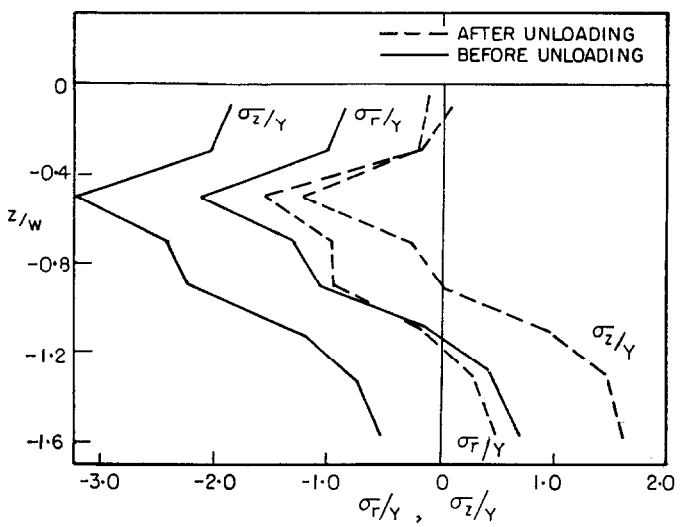
AFTER UNLOADING
BEFORE UNLOADING
σz/Y
σr/Y
z/w
0
-0·4
-0·8
-1·2
-1·6
-3·0
-2·0
-1·0
0
1·0
2·0
σr/Y , σz/Y

(b)

tensile up to the punch radius and became compressive with sharp changes in magnitudes; then they increased to tensile stresses toward the edge of the specimen.

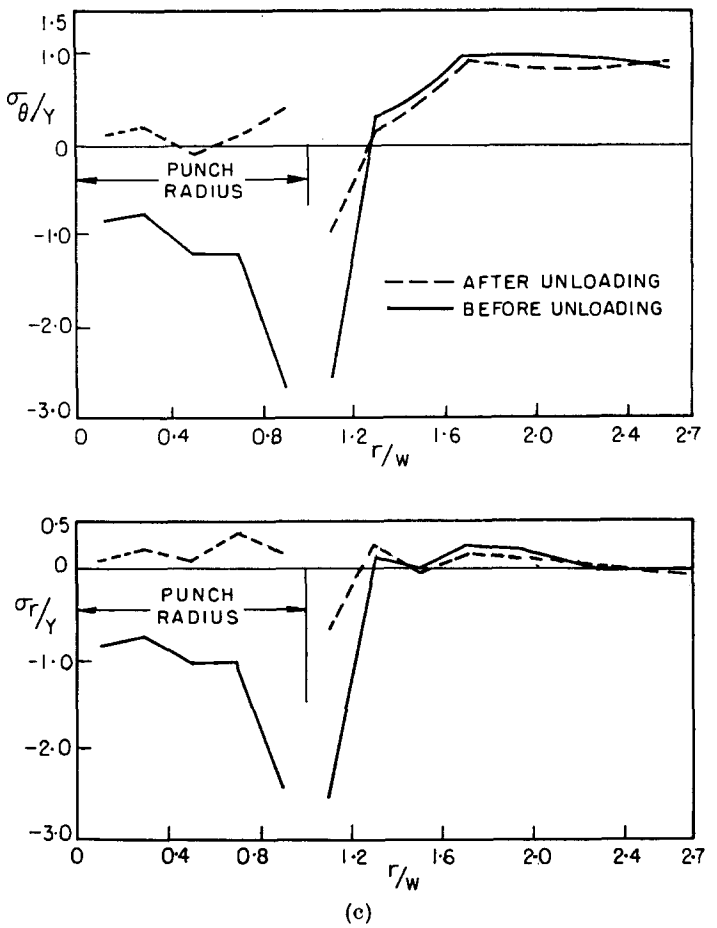

(c)

FIG. 18. Stress distributions after complete unloading. Same conditions as Fig. 17. (a) Along the contact surface with the foundation, (b) along the axis of symmetry and (c) along the top free surface.

CONCLUSIONS

For an analysis of elastoplastic problems, the finite-element method removes many restrictions imposed by other methods and offers a possibility of obtaining the information that the other methods could not provide. The method is applicable for complex geometry and takes into account realistic friction conditions and actual material properties. It reveals the elastic–plastic boundaries, the development of the plastic zone and the detailed stress and strain distributions. Furthermore, the problem of unloading and the calculation of residual stresses can be handled by this method. Most of these features were demonstrated in this paper for the problem of indentation. However, questions still remain with regard to the accuracy of the solutions and the efficiency of the computation.

Acknowledgements—The authors wish to thank the National Science Foundation for its grant GK-1775, under which the present investigation was made. They also wish to thank the Computer Center, University of California, Berkeley, for the use of computer facilities. They are indebted to Mrs. Naomi Troth for editing the manuscript, Miss LaVerne Marts for typing and Mr. W. Kot for preparing the figures.

REFERENCES

1. L. PRANDTL, *Nachrichten der Akademie der Wissenschaften, Göttingen, Mathematische-physikalische Klasse* 74 (1920).
2. R. RILL, *The Mathematical Theory of Plasticity*. Clarendon Press, Oxford (1950).
3. R. HILL, E. H. LEE and S. J. TUPPER, *Trans. ASME, J. appl. Mech.* **18**, 46 (1951).
4. A. P. GREEN, *Phil. Mag.* **42**, 900 (1951).
5. R. T. SHIELD, *Proc. R. Soc.* **A233**, 267 (1955).
6. M. C. SHAW and G. J. DESALVO, On the plastic flow beneath a blunt axisymmetric indenter. Presented at ASME Winter Annual Meeting, Los Angeles (1969).
7. M. C. SHAW and G. J. DESALVO, A new approach to plasticity and its application to blunt two-dimensional indenters. Presented at the ASME Winter Annual Meeting, Los Angeles (1969).
8. O. C. ZIENKIEWICZ and Y. K. CHEUNG, *The Finite Element Method in Structural and Continuum Mechanics*. McGraw-Hill, London (1967).
9. J. H. ARGYRIS, Continua and discontinua. Opening paper presented at the Conference on Matrix Methods in Structural Mechanics, AFIT, Ohio (1965).
10. R. H. GALLAGHER, J. PADLOG and P. P. BIJLAARD, *ARS Journal* **32**, 700 (1962).
11. G. POPE, The application of the matrix displacement method to non-linear problems. Paper presented at the Conference on Matrix Methods in Structural Mechanics, AFIT, Ohio (1965).
12. J. L. SWEDLOW and W. H. YANG, Stiffness analysis of elastoplastic plates. Graduate Aeronautical Laboratories, California Institute of Technology, AFRPL-TR-66-5 (1966).
13. P. V. MARCAL and I. P. KING, *Int. J. mech. Sci.* **9**, 143 (1967).
14. C. A. FELIPPA, Refined finite element analysis of linear and non-linear two-dimensional structures. Ph.D. Dissertation, University of California, Berkeley (1966).
15. Y. YAMADA, N. YOSHIMURA and T. SAKURAI, *Int. J. mech. Sci.* **10**, 343 (1968).
16. F. A. AKYUZ and J. E. MERWIN, *AIAA Journal* **6**, 1825 (1968).
17. Y. YAMADA, Y. YOKOUCHI and G. SASAOKA, Analysis of contact problems by matrix method. Proc. Nat. Symposium on Matrix Methods of Structural Analysis and Design, Society of Steel Construction of Japan, Tokyo (1969).
18. E. L. WILSON, A digital computer program for the analysis of axisymmetric solids with orthotropic nonlinear material properties. US Air Force Report No. BSD-TR-67-228 (1967).
19. W. P. DOHERTY, E. L. WILSON and R. L. TAYLOR, Report No. S.E.S.M. 69-3, Structural Engineering Laboratory, University of California, Berkeley, January (1969).
20. J. F. W. BISHOP, *J. Mech. Phys. Sol.* **6**, 132 (1958).